XMMU J050722.1–684758: Discovery of a new Be X-ray binary pulsar likely associated with the supernova remnant MCSNR J0507–6847

C. Maitra, F. Haberl, P. Maggi, P. Kavanagh, G. Vasilopoulos, M. Sasaki, M. Filipović, A. Udalski

Monthly Notices of the ROYAL ASTRONOMICAL SOCIETY

MNRAS **504,** 326–337 (2021) doi:10.1093/mnras/stab716
Advance Access publication 2021 March 18

XMMU J050722.1−684758: discovery of a new Be X-ray binary pulsar likely associated with the supernova remnant MCSNR J0507−6847

C. Maitra [1]★ F. Haberl,[1] P. Maggi,[2] P. J. Kavanagh,[3] G. Vasilopoulos [4] M. Sasaki [5] M. D. Filipović[6] and A. Udalski[7]

[1]*Max-Planck-Institut für extraterrestrische Physik, Gießenbachstraße, D-85748 Garching, Germany*
[2]*Université de Strasbourg, CNRS, Observatoire astronomique de Strasbourg, UMR 7550, F-67000 Strasbourg, France*
[3]*School of Cosmic Physics, Dublin Institute for Advanced Studies, 31 Fitzwillam Place, Dublin 2, Ireland*
[4]*Department of Astronomy, Yale University, PO Box 208101, New Haven, CT 06520-8101, USA*
[5]*Remeis Observatory and ECAP, Universität Erlangen-Nürnberg, Sternwartstr. 7, D-96049 Bamberg, Germany*
[6]*Western Sydney University, Locked Bag 1797, Penrith South DC, NSW 2751, Australia*
[7]*Astronomical Observatory, University of Warsaw, Aleje Ujazdowskie 4, PL-00-478 Warsaw, Poland*

Accepted 2021 March 3. Received 2021 February 19; in original form 2020 December 22

ABSTRACT

We report the discovery of a new high-mass X-ray binary pulsar, XMMU J050722.1−684758, possibly associated with the supernova remnant (SNR) MCSNR J0507−6847 in the Large Magellanic Cloud, using *XMM–Newton* X-ray observations. Pulsations with a periodicity of 570 s are discovered from the Be X-ray binary XMMU J050722.1−684758 confirming its nature as a HMXB pulsar. The HMXB is located near the geometric centre of the SNR MCSNR J0507−6847(0.9 arcmin from the centre) which supports the XRB-SNR association. The estimated age of the SNR is 43–63 kyr years which points to a middle aged to old SNR. The large diameter of the SNR combined with the lack of distinctive shell counterparts in optical and radio indicates that the SNR is expanding into the tenuous environment of the superbubble N103. The estimated magnetic field strength of the neutron star is $B \gtrsim 10^{14}$ G assuming a spin equilibrium condition which is expected from the estimated age of the parent remnant and assuming that the measured mass-accretion rate remained constant throughout.

Key words: Radiation mechanisms: general – ISM: supernova remnants – Magellanic Clouds – Radio continuum: ISM – X-rays: individuals: XMMU J050722.1−684758 – X-rays: individuals: MCSNR J0507−6847.

1 INTRODUCTION

A neutron star (NS) X-ray binary associated with its parent supernova remnant (SNR) is an extremely rare object and can provide unique insights on the early evolutionary stages of NSs in the presence of a binary companion. The visibility time of a SNR is only a few 10^4 yr, which is typically three orders of magnitude shorter than the lifetime of high-mass X-ray binaries (HMXBs). A HMXB-parent SNR association therefore implies a very young binary system. A majority of these associations have been found in the Magellanic Clouds (MCs) in recent years, given their ideal environment for hosting young stellar remnants, a high formation efficiency for HMXBs, as well as relatively small distance and low foreground absorption conducive to performing detailed studies.

Discovered XRB-SNR associations include LXP 4.4 (Maitra et al. 2019), SXP 1062 (Haberl et al. 2012; González-Galán et al. 2018), CXO J053600.0−673507 (Seward et al. 2012), SXP 1323 (Gvaramadze, Kniazev & Oskinova 2019) in the MCs, and SS 433 and Circinus X-1 in our Galaxy (Geldzahler, Pauls & Salter 1980; Heinz et al. 2013). The youngest among them until now are Circinus X-1, with an estimated age <4600 yr (Heinz et al. 2013) and LXP 4.4 with an estimated age of <6000 yr (Maitra et al. 2019).

MCSNR J0507−6847 is a candidate SNR in the LMC (Bozzetto et al. 2017) that was first reported by Chu et al. (2000) as RX J050736−6847.8, a large ring (∼150 pc) of diffuse X-ray emission projected in the vicinity of the superbubble LHA 120-N 103 (hereafter N103). Superbubbles are large structures in the interstellar medium created by the supernova explosions of massive stars and their stellar winds in an OB association or stellar cluster. The shock-heated gas in superbubbles emit in X-ray wavelengths. Detection of excess of diffuse X-ray emission in superbubbles are indicative of the presence of interior SNRs shocking the inner walls of the superbubble shell (see for e.g. Dunne, Points & Chu 2001).

The above category of SNRs expand in the low-density medium of the superbubble, and have very weak optical and radio emission associated with them. Therefore, the nature of these systems cannot be confirmed using the conventional SNR diagnostics, i.e. presence of a high [S II]/[Hα] line ratio and non-thermal radio emission coincident in X-ray emission. The candidate MCSNR J0507−6847 was likewise indicated to be the largest SNR in the LMC expanding in the low density environment of the superbubble N103, and hence with no discernible optical emission (MCELS) and radio continuum emission (Chu et al. 2000; Bozzetto et al. 2017; Yew et al. 2020). The X-ray luminosity of the system lies within the range expected

★ E-mail: cmaitra@mpe.mpg.de

Table 1. *XMM–Newton*observations details of XMMU J050722.1−684758.

Date yyyy/mm/dd	Observation ID	Exposure PN/MOS2/MOS1 (ks)	Off-axis angle PN/MOS2/MOS1 (arcmin)	Telecope vignetting PN/MOS2/MOS1
2000/07/07	0113000301	11.8/16.2 / 23.6	10.4/ 9.7/ 8.7	0.51 /0.48/0.52
2017/10/19	0803460101	53.0/55.0/55.0	10.0/11.1/11.1	0.52/0.54/0.55

for SNRs, and the age was estimated to be $\sim 5 \times 10^4$ yr based on the Sedov solution (Chu et al. 2000).

In this work, we identify for the first time the BeXRB XMMU J050722.1−684758 and MCSNR J0507−6847as a possible SNR-HMXB association and investigate the properties of the SNR and its compact object in detail. We report the discovery of pulsations from the BeXRB XMMU J050722.1−684758 located near the geometrical centre of the SNR candidate MCSNR J0507−6847. This confirms its nature as an NS. van Jaarsveld et al. (2018) identified the source as a BeXRB in the LMC with the optical companion classified as a B3 IIIe star and suggested a binary orbital period of 5.27 d. We identified a more likely orbital period of 40.2 d using more than 22 yr of OGLE monitoring data. The observations and their analysis are described in Section 2. Section 3 presents the results and Section 4 the discussion and Section 5 the conclusions.

2 OBSERVATIONS AND ANALYSIS

2.1 X-ray observations and analysis

XMMU J050722.1−684758 was observed serendipitously with *XMM–Newton* twice in 2000 (Observation 1 from now) and again in 2017 (Observation 2 from now). The observation details are given in Table 1. EPIC (Strüder et al. 2001; Turner et al. 2001) observations were processed with the *XMM–Newton* data analysis software SAS version 18.0.0.[1] We searched for periods of high background flaring activity by extracting light curves in the energy range of 7.0–15.0 keV and removed the time intervals with background rates $\geq$ 8 and 2.5 count ks^{-1} arcmin^{-2} for EPIC-PN and EPIC-MOS, respectively (Sturm et al. 2013). Events were extracted using the SAS task `evselect` by applying the standard filtering criteria (`#XMMEA_EP && PATTERN< = 4` for EPIC-PN and `#XMMEA_EM && PATTERN< = 12` for EPIC-MOS).

The *Swift*/XRT data were analysed following the *Swift* data analysis guide[2] (Evans et al. 2007). Because of the low flux of XMMU J050722.1−684758 in all observations, we only performed a simple source detection and position determination using a sliding-cell detection algorithm implemented by `XIMAGE and sosta`.[3] For non-detections, we estimated the 3σ upper limits using a Bayesian method introduced by Kraft, Burrows & Nousek (1991).

2.2 OGLE

The infrared counterpart of the HMXB XMMU J050722.1−684758 is identified to be 2MASS 05072214−6847592with *J*, *H*, and *K* magnitudes of 15.0, 15.3, and 14.6 mag respectively. 2MASS 05072214−6847592 was observed by the Optical Gravitational Lensing Experiment (OGLE), which started observations in 1992 (Udalski et al. 1992) and continued observing until today (OGLE-IV, Udalski, Szymański & Szymański 2015), but interrupted since March 2020. Optical observations were performed with the 1.3-m Warsaw telescope at Las Campanas Observatory, Chile. Images are taken in the V and I filter passbands and photometric magnitudes are calibrated to the standard VI system.

3 RESULTS

3.1 Morphology of MCSNR J0507−6847

Figs 1 and 2 display the combined *XMM–Newton* EPIC image centered on MCSNR J0507−6847overlaid with optical (MCELS) and radio (ASKAP) contours. The source morphology resembles a large circular shell-like structure of diffuse emission of $\sim$150 pc in diameter. It is projected in the vicinity of the superbubble N103 adjacent to SNR N103B (MCSNR J0508–6843) in the east (Maggi et al. 2016; Bozzetto et al. 2017). The north-eastern part of the shell overlaps with the hot gas of the superbubble which is also indicated by the presence of strong optical Hα and radio-continuum emission coincident with this region. The south-western shell is more clearly defined. No optical or radio emission is detected from the shell region which is possibly due to the fact that MCSNR J0507−6847 expands in the low-density environment of the superbubble. To measure the size of the shell, we employed the method described by Kavanagh et al. (2015), which fits an ellipse to the outer contours of the shell (at 3σ above the surrounding background level in the 0.2−1 keV EPIC image). Due to the contamination of the northern shell region with the SB N103 as seen from the Hα contours in Fig. 2, the extended emission from the north is used as a background component to define the contour around the northern shell. We derive the ellipse centre at RA $= 05^{\rm h}07^{\rm m}32\overset{\rm s}{.}1$ and Dec. $= -68^{\circ}47'40\overset{''}{.}7$(J2000). The semi-major and semi-minor axes of $5.32'(\pm\ 0.21')$ and $4.84'(\pm\ 0.21')$, respectively, correspond to a size of 154.6 × 140.8 ($\pm$6.1) pc at the distance of the LMC (50 kpc) with the major axis rotated $\sim 49\overset{\circ}{.}3$ East of North.

3.2 Identification of point sources inside the shell

In order to identify the point sources, we performed a maximum-likelihood source detection analysis on the *XMM–Newton*/EPIC images on 15 images created from the three EPIC cameras in five energy bands as given in (Watson et al. 2009; Sturm et al. 2013). Source detection was performed simultaneously on all the images using the SAS task `edetect_chain`. Two point-like sources are found near the centre of the shell morphology. The source to the east is identified as a spectroscopically confirmed quasar MQS J050736.44−684751.6 with $z = 0.53$ (Souchay et al. 2012; Kozłowski et al. 2013) and is hence a background object which is projected in the line of sight of MCSNR J0507−6847.

[1]Science Analysis Software (SAS): http://xmm.esac.esa.int/sas/
[2]http://www.swift.ac.uk/analysis/xrt/
[3]https://heasarc.gsfc.nasa.gov/xanadu/ximage/ximage.html

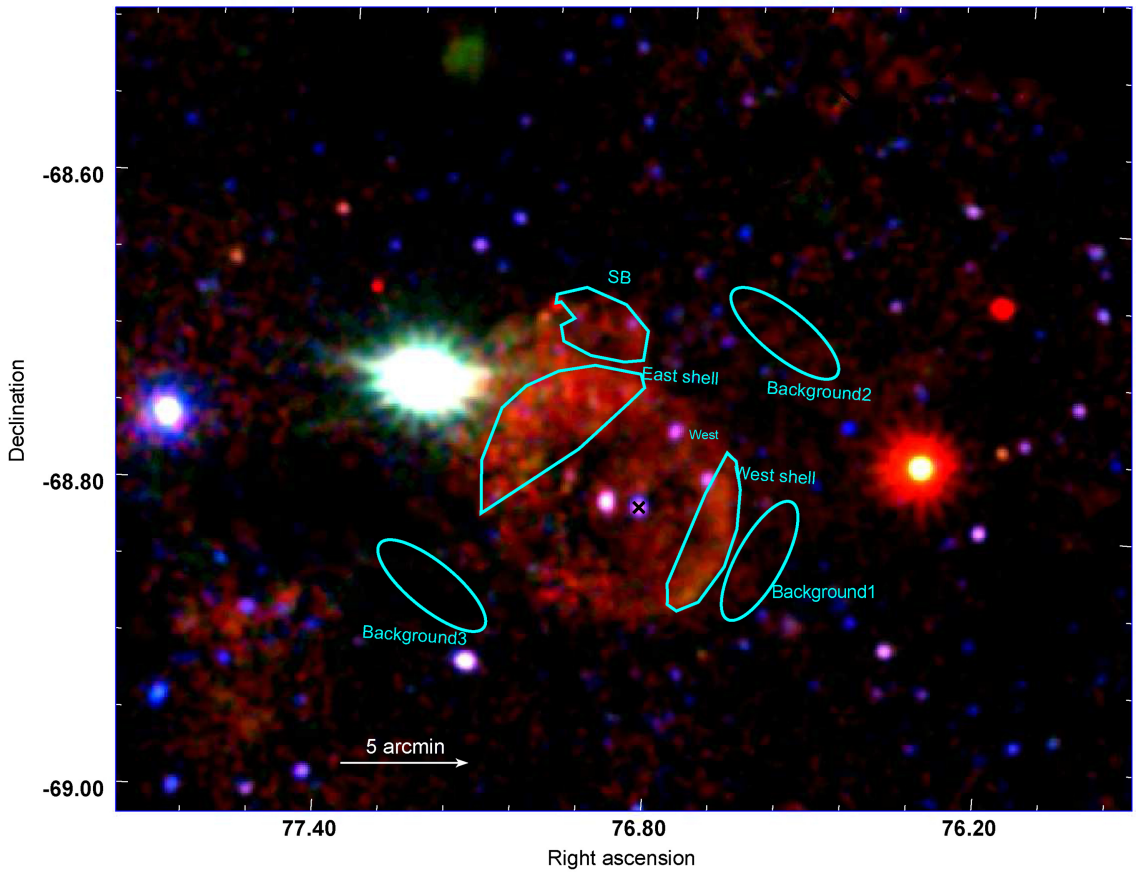

Figure 1. *XMM–Newton* EPIC RGB (R= 0.3–0.7 keV, G= 0.7–1.1 keV, B = 1.1–4.2 keV) image of XMMU J050722.1−684758. The regions used for spectral extraction are shown in cyan. The black cross shows the optical position of the BeXRB.

The other point-source marked with black cross in Fig. 1 and magenta cross in Fig. 2 lies 0.9 arcmin away from the geometric centre of the SNR. Its best-determined position is RA $= 05^{h}07^{m}22\overset{s}{.}37$ and Dec. $= -68^{\circ}47'58\overset{''}{.}2$ with a 1σ statistical uncertainty of 0.72 arcsec. The positional error is dominated by systematic astrometric uncertainties and a systematic error of 0.37 arcsec was added in quadrature (Rosen et al. 2016). The source was already identified as a BeXRB in the LMC from optical spectroscopic observations (BeCand 3 in van Jaarsveld et al. 2018). The confirmation of the nature of the source as an NS (see later section) and its positional proximity to the geometric centre of the SNR indicates that it is the compact object born out of the explosion of MCSNR J0507−6847. We calculated the probability of chance coincidence for a HMXB pulsar to lie within 0.9 arcmin of the centre of an SNR within the LMC. For this, we used the total of 21 known HMXBs with detected pulsations and ∼57 confirmed SNRs (with sizes that can be resolved with *XMM–Newton*) to be identified within the *XMM–Newton* observations of the LMC which cover an area of ∼20 deg^2 in total. Assuming that the HMXBs and SNRs are uniformly distributed within the survey area, the probability of finding a HMXB by chance within 0.9 arcmin of the centre of an SNR is 0.04. It is to be noted that HMXBs and core-collapse SNRs (which constitute about 60 per cent of all LMC SNRs, Maggi et al. 2016) are not uniformly distributed but follow star-forming regions, so this probability is likely underestimated. The probability of chance coincidence would also be slightly higher if all known HMXBs in the LMC are taken into account. The low-probability supports the association of the HMXB with the SNR, but a chance coincidence can formally not be ruled out.

3.3 OGLE monitoring of the optical counterpart

3.3.1 Long-term OGLE I-band light curve

Fig. 3 shows the OGLE I-band light curve of the optical counterpart of XMMU J050722.1−684758 obtained during observing phases II-IV over a period of 13 yr. The light curve is variable in nature showing dip-like features, typical of Be stars with a binary companion. The average I band magnitude of the source is 15.8 mag. In order to verify the orbital period of the system, we detrended the light curve by subtracting a smoothed light curve (derived by applying a Savitzky–Golay filter with a window length of 101 data points, Savitzky & Golay 1964) and computed Lomb–Scargle peridograms (Lomb 1976; Scargle 1982). A highly significant peak is found in the periodogram at 5.266 d with two other peaks at 1.235 and 40.16 d (Fig. 4). The 1.235 and 5.266-d periods (frequencies of 0.810 and 0.190 d^{-1}, respectively) are aliases of each other with the 1-d sampling period of the light curve. Since short periods near 1 d are most likely caused by non-radial pulsations of the Be star (e.g. Schmidtke, Cowley & Udalski 2013), we suggest the 40.16-d period as the most likely orbital period of the system, which is also more typical for BeXRBs (Haberl & Sturm 2016). The detrended light-curve folded with that period is presented in Fig. 5.

3.3.2 OGLE V-band and colour variations

During OGLE phases III and IV also *V*-band measurements of the optical counterpart of XMMU J050722.1−684758 are available, in

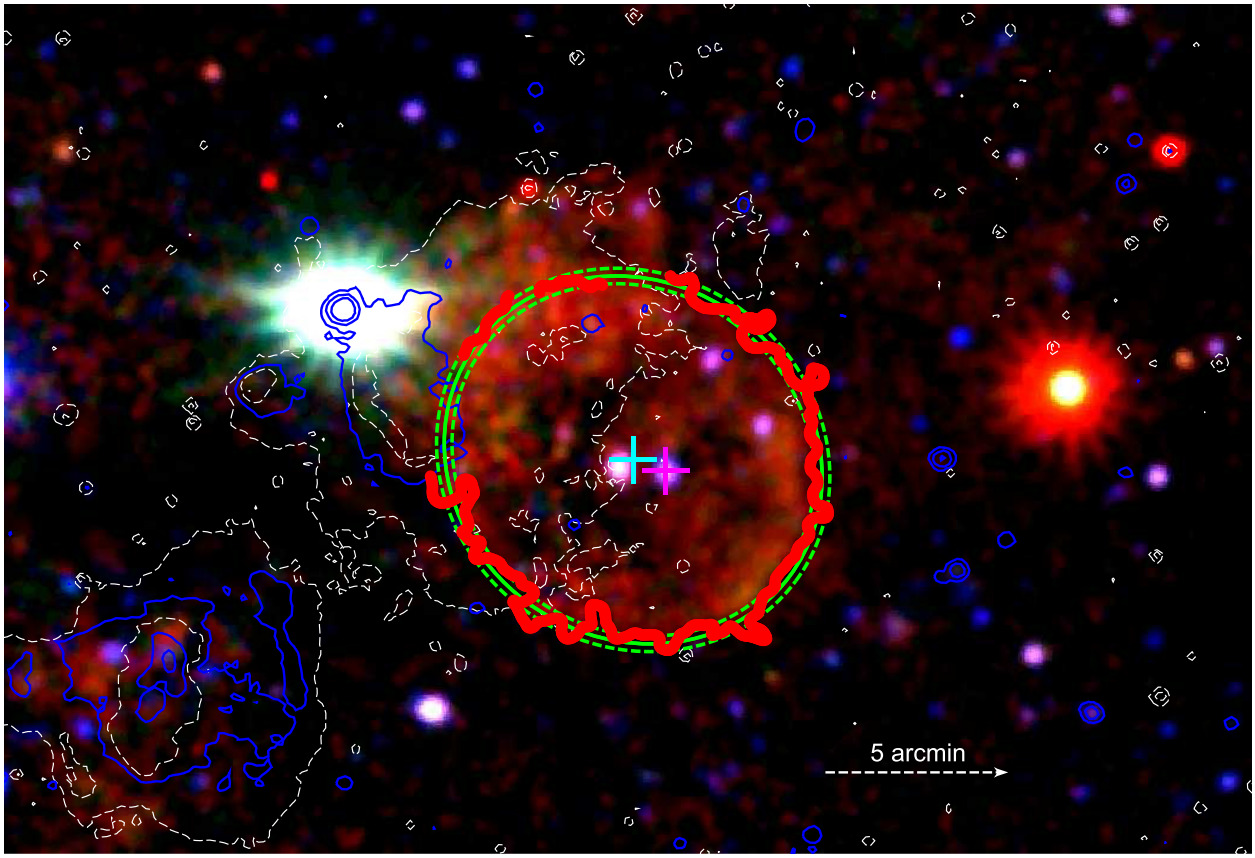

Figure 2. Zoomed in *XMM–Newton* EPIC RGB (R= 0.3–0.7 keV, G= 0.7–1.1 keV, B = 1.1–4.2 keV) image of XMMU J050722.1−684758. Overlaid in blue are radio contours from the latest Australian Square Kilometre Array Pathfinder (ASKAP) survey of the LMC at 888 MHz (bandwidth is 288 MHz). The radio continuum contours correspond to 1, 2, and 3 mJy beam^{-1} while the image beam size is 13.7 × 11.8 arcsec^2 and local rms is ∼0.2 mJy beam^{-1}. The white line overlays the Hα image contours from the Magellanic Clouds Emission Line Survey (MCELS) (Smith et al. 2004). The cyan cross shows the best-fitting centre of the SNR and the magenta cross the position of the optical counterpart of the BeXRB. The red solid line indicate the X-ray contour level corresponding to 3σ above the average background surface brightness. The green solid line shows the best-fitting ellipse to the contour, with the dashed lines denoting the 1σ errors on the best fit.

particular, around the sharp drop in brightness around MJD 56200 d (Figs 3 and 6). We created I-V colour indices by using the measured *V*-band magnitudes and neighbouring *I*-band values interpolated to the time of the *V*-band measurement. The colour–magnitude diagram is shown in Fig. 7.

3.4 X-ray timing analysis

XMMU J050722.1−684758 displayed a net count rate (PN) of 0.03 count s^{-1} during Observation 1 and 0.05 count s^{-1} during Observation 2 in the energy range of 0.2–12 keV confirming its variable nature. The X-ray light curves during the individual observations however did not exhibit variability on shorter time-scales. Since the source was brighter during Observation 2 and was observed for a longer duration, data from this observation was considered to study the temporal properties of the source in detail. To look for a possible periodic signal in the X-ray light curve of the HMXB, we extracted source events using a circular region with radius 26 arcsec centred on the best-fit position, and a background region of a larger size away from the source as shown in Fig. 1. The light curve was corrected for all effects like vignetting and Point Spread Function losses by the task `epiclccorr`. At first, we searched for a periodic signal in the barycentre-corrected *XMM–Newton* EPIC light curve in the energy range above 1 keV using a Lomb–Scargle periodogram analysis in the period range of 0.5–3000 s (Lomb 1976; Scargle 1982). A strong periodic signal is detected at 570.4 s indicating the spin period of the NS in the BeXRB (Fig. 8). In order to determine the pulse period more precisely, we employed the Bayesian periodic signal detection method described by Gregory & Loredo (1996). The spin period and its associated 1σ error are determined to 570.35 ± 0.35 s. The spin period and its associated *XMM–Newton* EPIC light curve in the range of 1–12 keV, folded with the best-obtained period is shown in Fig. 9. The pulse fraction in the same energy range is 40 per cent and no change in the pulse shape or pulse fraction can be detected within this energy range. Pulsations cannot be detected below 1 keV, possibly due to the contamination from the SNR.

The source was scanned 49 times during the first all-sky survey (eRASS1) of the eROSITA instrument (Predehl et al. 2020) on board the Russian/German Spektrum–Roentgen–Gamma (SRG) mission. The scans spanned between MJD 58980.53 to MJD 58987.09, accumulating a total exposure of 1543 s. The source was variable during the scans and the count rates remained around 0.08 ± 0.03 count s^{-1} (0.2–8.0 keV) around MJD 58981.54 in the beginning and dropped to < 0.01 count s^{-1} towards the end of the eRASS1 scans. Source detection was performed simultaneously on all the images in the standard eROSITA energy bands of 0.2–0.6, 0.6–2.3, and 2.3–5.0 keV. The vignetting and point spread function corrected count rate in the energy range of 0.2–5.0 keV was 0.05 ± 0.01 count s^{-1}

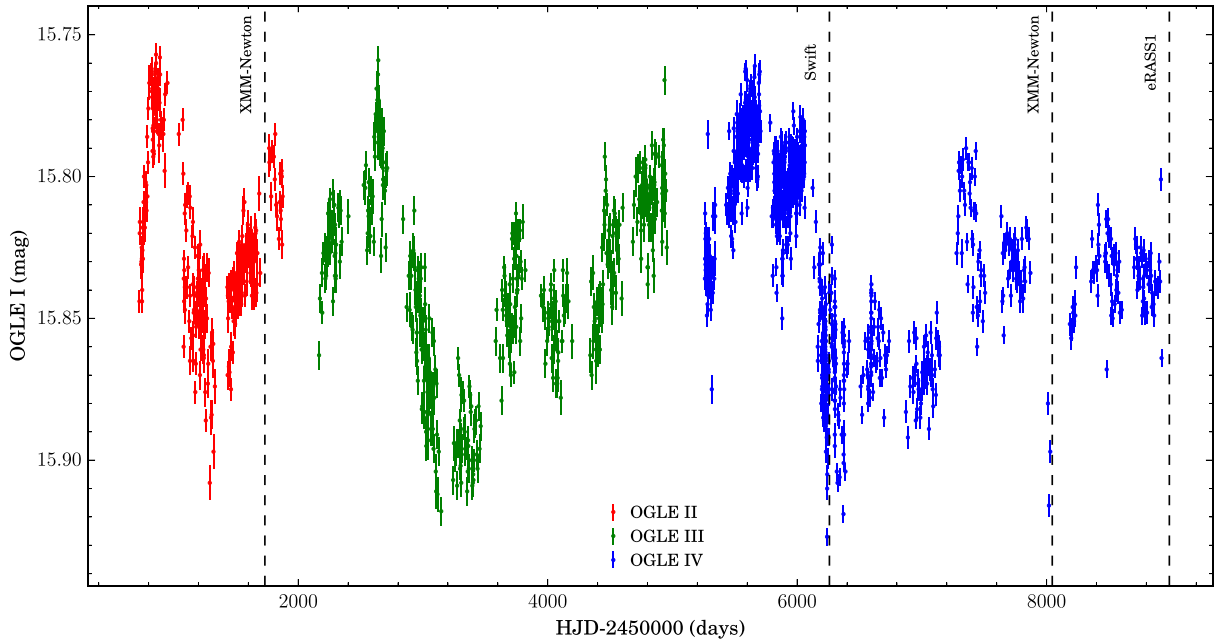

Figure 3. OGLE *I*-band light curve of 2MASS 05072214−6847592 from 1997 October to 2020 March. Epochs of X-ray observations analysed in this work are marked with vertical dashed lines.

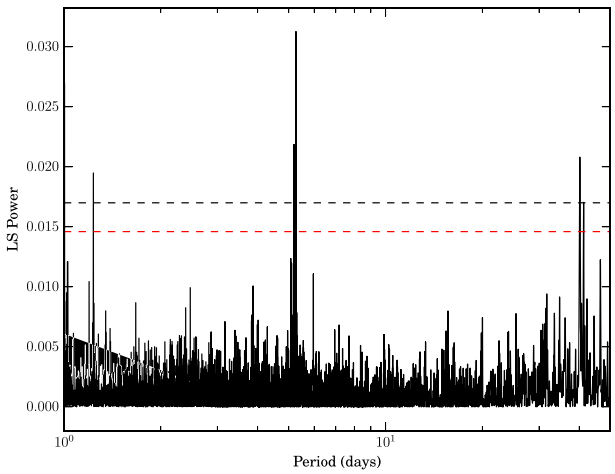

Figure 4. Lomb–Scargle periodogram of the detrended OGLE *I*-band light curve of 2MASS 05072214−6847592. Significant peaks are found at 1.235, 5.266, and 40.16 d. The red and black dashed lines mark the 95 and 99 per cent confidence levels, respectively.

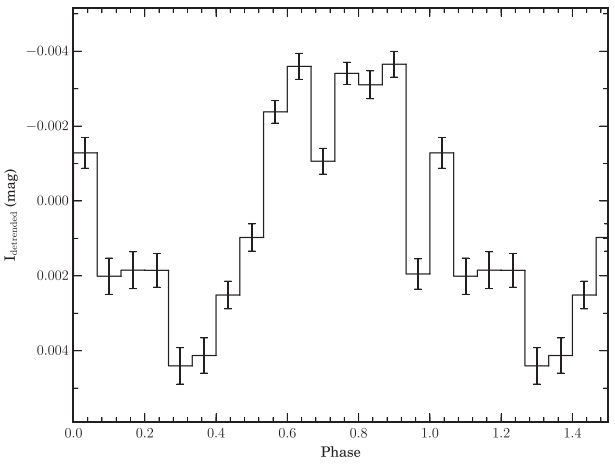

Figure 5. Detrended OGLE *I*-band light curve folded with a period of 40.1609 d.

indicating a similar average flux as observed during *XMM–Newton* Observation 2.

3.5 X-ray spectral analysis

For the spectral analysis, the SAS tasks `rmfgen` and `arfgen` were used to create the redistribution matrices and ancillary files. The significant extent of the SNR and varying off-axis position in the two observations was taken into account by extracting spectra from vignetting-weighted event lists, created through the SAS task `evigweight` (as described in Maggi et al. 2016). To account for the spatially dependent non-X-ray background (NXB) in extended emission spectra, spectra were extracted from Filter Wheel Closed (FWC) data at the same detector position. Spectra were binned to achieve a minimum of 20 and 25 counts per spectral bin for the point source and SNR, respectively, to allow using the χ^2 statistic. The spectral analysis was performed using the XSPEC fitting package, version 12.9 (Arnaud 1996). Errors were estimated at the 90 per cent confidence level, unless otherwise stated.

3.5.1 MCSNR J0507−6847

Spectra were extracted from the entire shell region, from the eastern and western hemispheres, and from the superbubble region to the North (see Fig. 1). Background spectra were accumulated in nearby regions chosen individually per instrument and observation. In Observation 1, we also made sure to exclude a large region around the bright SNR N103B and its streak of out-of-time events. Point sources detected in the background and shell region, including the background AGN and HMXB, were excised using circular regions

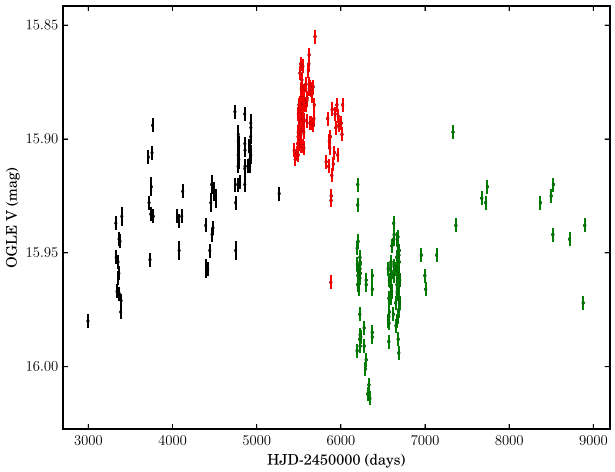

Figure 6. OGLE *V*-band light curve of 2MASS 05072214−6847592. The colours mark different phases of brightness and colour evolution as shown in Fig. 7.

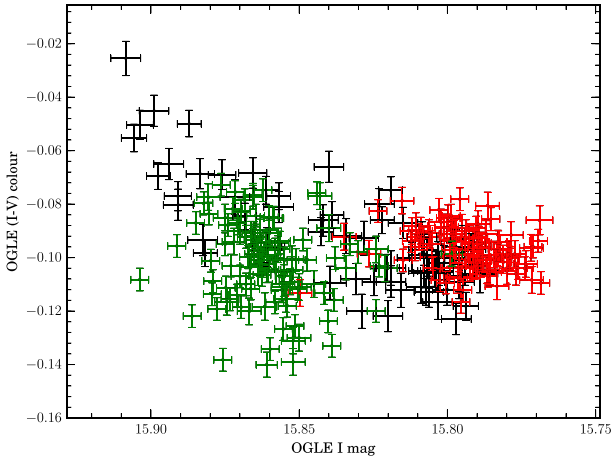

Figure 7. OGLE colour(I–V)–magnitude(I) diagram of 2MASS 05072214−6847592. During brightness rise (black) the emission becomes redder reaching asymptotically a minimum value in I–V (red), which is also maintained after the brightness drop (green).

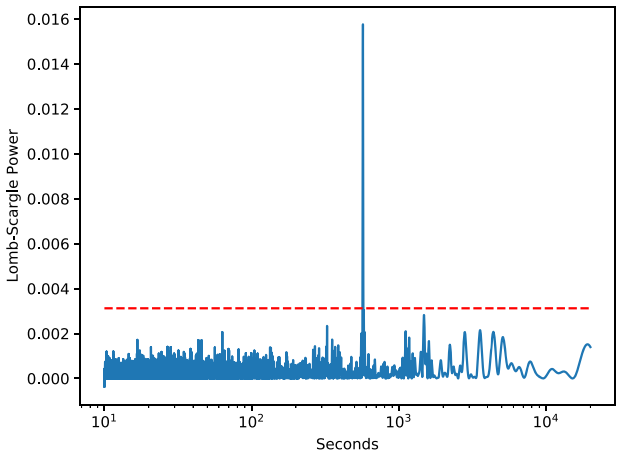

Figure 8. Lomb–Scargle periodogram of the *XMM–Newton* EPIC light curve in the energy band of 1–12 keV (Observation ID 0803460101). The peak indicates the spin period of the NS. The red dashed line mark the 99.73 per cent confidence levels.

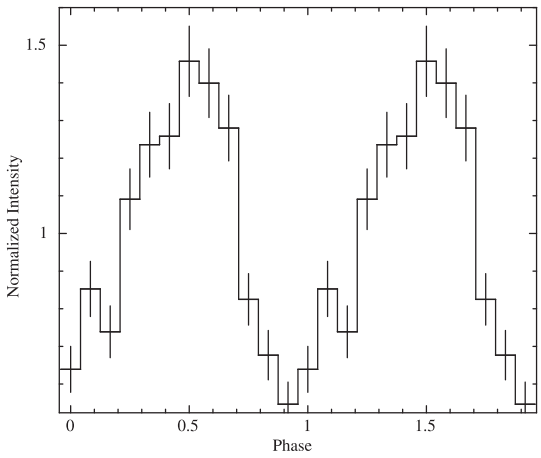

Figure 9. Corrected EPIC-PN light curve folded with 570.35 s, showing the pulse profile of the HMXB in the energy band of 1–12 keV.

with a 25 arcsec radius. Thus, we estimated that < 5 per cent of the source counts from these sources will contaminate our extended source spectra due to PSF leaks. Source and background spectra were fitted simultaneously, with NXB parameters tied to those obtained from the FWC spectra, and astrophysical X-ray background (AXB) parameters constrained from background spectra. The AXB comprises Galactic thermal emission (local hot bubble, Galactic halo), cosmic X-ray background, and LMC diffuse emission. More details on this method can be found in Maggi et al. (2016, 2019).

The X-ray absorption was modelled using the `tbabs` model (Wilms, Allen & McCray 2000) with atomic cross-sections adopted from Verner et al. (1996). We used two absorption components: The first one to describe the Galactic foreground absorption, where we used a fixed column density of 6×10^{20} cm^{-2} (Dickey & Lockman 1990) with abundances taken from Wilms et al. (2000). The second component accounts for the LMC material in front of the object. For the latter absorption component, the abundances were set to LMC abundances following Maggi et al. (2016) and the column density $N_{\rm H}^{\rm LMC}$ was free in the analysis. The cosmic X-ray background, seen through all the LMC, was absorbed by the total line-of-sight column density of 2.0×10^{21} cm^{-2}, obtained from the ATCA + Parkes map of Kim et al. (2003) averaged over 0.1 deg^2.

We fit the X-ray spectra with collisional ionization equilibrium and non-equilibrium ionization thermal emission models (XSPEC models `vapec` and `vpshock`, respectively), typical for shock-heated plasma in SNRs. We also attempted to fit the abundances of the main elements in the energy range of the SNR emission, namely O, Ne, Mg, and Fe. However, meaningful constraints were only obtained for the entire shell spectrum and not for the smaller regions due to limited statistics. For these spectra and all other elements, abundances were fixed to that of the LMC hot gas. Best-fitting spectral parameters are listed in Table 3 and the spectra with the best-fitting model in Fig. 10. Improvements to the fit quality with the non-equilibrium ionization model were only marginal. Regardless of ionization equilibrium status, the overall absorption is low, indicating an object on the nearer side of the LMC gaseous disc. As expected from the X-ray images and dearth of emission at $E \gtrsim 1$ keV, the plasma temperature is relatively low, at $kT < 0.4$ keV.

Table 2. *Swift* observations details of XMMU J050722.1−684758.

Date	Observation ID	Mode	Exposure (s)	Observed luminosity
55962.8	00045577002	PC	2128	<8.6
55994	00045444002	PC	248	<77.3
56252.5	00045444003	PC	779	<37.8
56254.9	00045444004	PC	904	<28.8
56259.3	00045444005	PC	1116	56.7
56377.8	00045576001	PC	2872	<6.9
56968.9	00033486001	PC	961	<14.4
56972.2	00033486002	PC	434	<31.8
57109.2	00033486003	PC	439	<31.5
57653	00034730001	PC	1101	<18.4
58220.5	00094089001	PC	247	<55.9
58234.3	00094089003	PC	243	<57.1
58255.6	00094089004	PC	245	<56.5
58262.3	00094089005	PC	247	<55.9
58290.9	00094089007	PC	245	<56.5
58332.6	00094089009	PC	250	<55.4
58346.8	00094089010	PC	245	<56.5
58360.7	00094089011	PC	232	<59.5
58374.7	00094089012	PC	250	<55.4
58388.5	00094089013	PC	240	<57.7
58416.8	00094089014	PC	242	<57.1
59006.9	00034730003	PC	1925	<11.6

[a]Luminosity in the 0.5–10 keV band in units of 10^{34} erg s^{-1}. [b]To convert *Swift*/XRT count rates to luminosities, we used the spectral parameters obtained from the fit to the *XMM–Newton* data. The conversion factor is 2.1×10^{37} erg s^{-1} (count s)$^{-1}$. Only *Swift* exposures of ≥ 200 s covering the source have been used for this purpose.

No strong spatial variations can be identified, all the parameters being consistent between eastern and western part of the shell, within the larger uncertainties stemming from the reduced statistics of the smaller regions. The emission from the superbubble region cannot be distinguished as well for the same reason as given above. With both the `vapec` and `vpshock` models, the abundances of O, Ne, Mg, and Fe and their ratios are the same: They are those of the LMC hot gas phase (Maggi et al. 2016; Schenck, Park & Post 2016) and reveal no enhancement by SN ejecta.

The total observed luminosity in the 0.3–8 keV band is $2.2(\pm 0.06) \times 10^{35}$ erg s^{-1}, lower than reported in Chu et al. (2000), likely because we measured a slightly lower plasma temperature and higher $N_{\rm H}$ (with better spectral resolution than *ROSAT*) and excluded point sources previously unresolved. This sets MCSNR J0507−6847among the brightest third of LMC SNRs (Maggi et al. 2016). However, given the large extent, the source is in the 20 per cent *faintest* SNRs when comparing surface brightness, which is the limiting factor for the study of extended sources.

3.5.2 HMXB

As in the case of the X-ray timing analysis, only data from Observation 2 were of sufficient statistical quality to perform a detailed spectral analysis. The X-ray spectrum of the HMXB XMMU J050722.1−684758 contains some contribution from the overlapping extended SNR as can be seen from Fig. 1. In order to model this contribution, we included a component for the SNR emission in the spectral fit with the normalization component left free – since the surface brightness of the SNR is not uniform, we do not constrain the contamination level to the fractional geometric area covered by the source extraction region. The X-ray spectrum of the HMXB can be satisfactorily modelled with an absorbed power law. The absorption scheme was the same as for the SNR, but the column density for the HMXB, $N_H^{\rm local}$, represents both LMC gas in front of thscenario: (i) the main NGC 1850e source and potential local contributions.

The spectral parameters for the best-fitting model using an absorbed power law are listed in Table 4 and the spectra and best-fitting model are shown in Fig. 11. The source was detected with an average absorption-corrected luminosity of 9×10^{34} erg s^{-1}. Assuming that the source exhibited a similar spectrum during Observation1 and from the PN count rate, we estimated an absorption corrected luminosity of 7×10^{34} erg s^{-1} for XMMU J050722.1−684758 during Observation 1.

The local absorption component $N_H^{\rm local}$ measured in the case of XMMU J050722.1−684758 is significantly higher than that measured for the SNR (see Table 4). In order to estimate the total amount of absorption column density towards the direction of the source, we extracted the spectrum from the quasar MQS J050736.44–684751.6 which overlaps with the SNR along the line of sight (Fig. 1). The spectrum was well fitted by an absorbed power law taking into account the determined redshift of the source. The best-fitting parameters correspond to $\Gamma = 2.3^{+0.2}_{-0.3}$ and $N_{\rm H} = 3 \times 10^{21}$ cm^{-2}. This is only slightly higher than the average integrated LMC column (2.0×10^{21} cm^{-2}, Section 3.5.1), perhaps due to further contribution by the host galaxy or intrinsic to the AGN. Nevertheless, this is several times lower than estimated from the HMXB XMMU J050722.1−684758 which

Table 3. X-ray spectral parameters of MCSNR J0507−6847.

Region	$N_H^{\rm LMC}$ (10^{20} cm^{-2})	kT (keV)	$\tau = n_{\rm e}\,t$ (10^{11} cm^{-3} s^{-1})	O	Ne	Mg	Fe	EM[a] (10^{57} cm^{-3})	χ^2/dof (χ^2_r)
				`vapec` parameters					
Shell	$7.1^{+4.2}_{-3.5}$	0.25 ± 0.01	—	$0.27^{+0.10}_{-0.07}$	$0.38^{+0.16}_{-0.10}$	$0.63^{+0.37}_{-0.24}$	$0.12^{+0.05}_{-0.03}$	$1.21^{+0.48}_{-0.38}$	2156.4/2051 (1.05)
East	0.8 (< 5.5)	0.22 ± 0.01	—			—		$0.98^{+0.29}_{-0.11}$	154.7/140 (1.11)
West	3.3 (<12.7)	0.23 ± 0.01	—			—		$0.89^{+0.40}_{-0.18}$	225.3/213 (1.06)
SB	0.0 (<7.6)	0.23 ± 0.03	—			—		0.53 ± 0.12	92.5/88 (1.05)
				`vpshock` parameters[b]					
Shell	0.0 (<1.3)	$0.36^{+0.07}_{-0.03}$	$6.3^{+8.1}_{-3.4}$	$0.30^{+0.04}_{-0.05}$	$0.40^{+0.07}_{-0.03}$	0.44 ± 0.16	0.11 ± 0.02	$0.49^{+0.13}_{-0.12}$	2148.6/2050 (1.05)
East	0.0 (<1.6)	$0.77^{+0.43}_{-0.21}$	$0.3^{+0.2}_{-0.1}$			—		$0.14^{+0.03}_{-0.02}$	149.9/139 (1.08)
SB	0 (<39.9)	$0.88^{+1.57}_{-0.46}$	$0.2^{+0.6}_{-0.1}$			—		$0.07^{+0.51}_{-0.02}$	90.2/87 (1.04)

[a]The emission measure $EM = n_{\rm e} n_{\rm H} V$, the product of electronic and proton densities with the total emitting volume, acts as a (temperature-dependent) normalization of thermal plasma models.
[b]The ionization time-scale could not be constrained for the West region, and thus we do not report `vpshock` parameters for it.

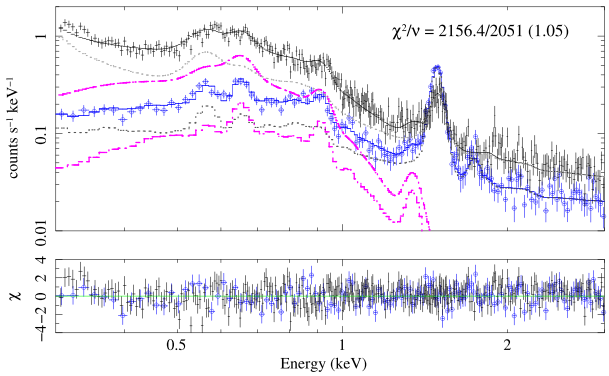

Figure 10. X-ray spectra of the SNR MCSNR J0507−6847. The upper panel shows the simultaneous spectral fit using all the available data (Table 1). For the sake of clarity only PN and MOS2 data from Observation id 0803460101 are displayed in black dots and blue circles, respectively. The total background models for PN and MOS are shown by the dotted grey lines. The best-fitting `vapec` model for the SNR emission is shown by the dashed magenta lines, as convolved with the PN and MOS spectral responses (top and bottom curves, respectively). The lower panel displays the residuals after the fit.

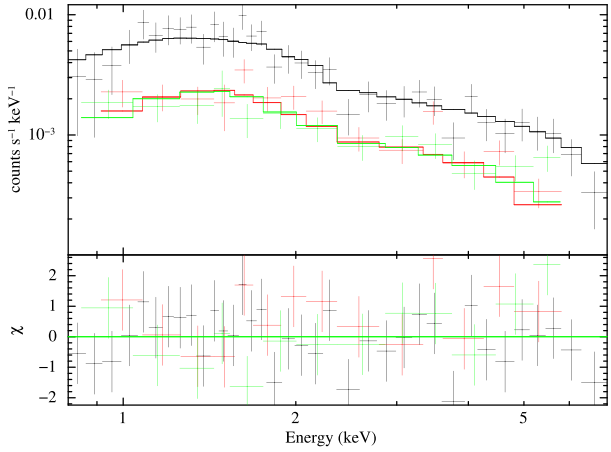

Figure 11. EPIC spectra of the HMXB XMMU J050722.1−684758. Black, red and green denotes PN, MOS1 and MOS2 data points and model (histogram), respectively. The spectra have been rebinned for visual clarity.

is very close to the quasar in projection. This establishes that the absorption of XMMU J050722.1−684758 is not originating from the LMC large-scale structure. Instead, it indicates that $N_{\rm H}^{\rm local}$ is dominated by a local absorbing column density as is often detected in the case of HMXBs in the MCs (Vasilopoulos et al. 2013; Coe et al. 2015; Maitra et al. 2018).

4 DISCUSSION

We report here the positional coincidence of the BeXRB XMMU J050722.1−684758 near the geometrical centre of MCSNR J0507−6847 and the possible association of the two sources. We performed detailed timing and spectral analysis of the BeXRB using *XMM–Newton*, *Swift*, eROSITA, and OGLE data and confirmed its nature as a highly magnetized NS. We also performed detailed X-ray spectral analysis of MCSNR J0507−6847 using *XMM–Newton* observations and compared with optical and radio observations to understand its nature.

Table 4. X-ray spectral parameters of the HMXB XMMU J050722.1−684758 for a power-law model.

Parameter	Value
$N_{\rm H}^{\rm local}$ (10^{22} cm^{-2})	$0.6^{+0.4}_{-0.3}$
Γ	1.2 ± 0.2
Flux[a] (0.2–12.0 keV)	2.6 ± 0.3
Flux (unabsorbed)[a] (0.2–12.0 keV)	3.0 ± 1.0
Absorption corrected X-ray luminosity[a] (erg s^{-1})	$8.5 \pm 1.0 \times 10^{34}$
χ^2	58.02
Degrees of freedom	59

[a]Flux in units of 10^{-13} erg cm^{-2} s^{-1} and assuming a distance of 50 kpc in the energy band of 0.2–12 keV .
[b]Absorption in units of 10^{22} cm^{-2} line-of-sight Galactic absorption was fixed to 6×10^{20}cm^{-2}.
[c]Errors are quoted at 90 per cent confidence.

4.1 Nature of XMMU J050722.1−684758: a BeXRB pulsar in the LMC

Using the latest *XMM–Newton* observation where the source was in the field of view (Observation 2), we discovered highly significant pulsations at 570 s which confirm the nature of XMMU J050722.1−684758 as a new BeXRB pulsar in the LMC. A total of ∼60 (candidate) HMXBs are known in the LMC out of which ∼90 per cent are Be/X-ray binaries and the rest are supergiant systems (Maitra et al. 2021; Haberl et al. 2020; Maitra et al. 2020, 2019; van Jaarsveld et al. 2018; Vasilopoulos et al. 2018; Antoniou & Zezas 2016). Pulsations have been detected from only a small fraction of them (21) until now. This source significantly improves our knowledge of BeXRB pulsars in the LMC especially due to its possible association with SNR MCSNR J0507−6847which allows an estimate of its age. The X-ray intensity varies on long time-scales as seen by comparing the *Swift* observations in Table 2. The eRASS1 scans also displayed variability on shorter time-scales

The optical light curve of XMMU J050722.1−684758 in the *I*-band spanning 13 yr is highly variable in nature showing dip-like features as is typical for Be stars with binary companion. An intriguing fact is that the *XMM–Newton* Observation 2 and the *Swift* detection fall into 'dips' in the optical emission as seen from the *I*-band light curve. The I versus V–I colour−magnitude evolution displays that the emission becomes redder during the rise of the optical brightness, and asymptotically reaches a minimum value in I–V colour. This indicates that as the Be disc grows in size, the optical emission gets brighter while the red continuum increases, a behaviour similar to what is seen in other MC BeXRBs (e.g. Haberl et al. 2017; Vasilopoulos et al. 2014; Coe et al. 2012)

4.2 Nature and properties of MCSNR J0507−6847

The shell-like morphology of MCSNR J0507−6847combined with its X-ray spectrum is typical of an middle-aged to old SNR. What sets it apart is its extreme diameter of 150 pc, easily the largest when compared to the population of confirmed LMC SNRs (the largest SNR in Bozzetto et al. 2017, is 128×82 pc^2). Combined with the lack of obvious shell counterparts in optical and radio, the most natural explanation of the properties of MCSNR J0507−6847 is that it is indeed an SNR, but expanding into a very tenuous environment.

One can estimate properties such as ambient density, explosion energy, and age of the SNR based on its morphological and spectral parameters, under the assumption that it is in the Sedov phase (e.g. van der Heyden, Bleeker & Kaastra 2004; Maggi et al. 2012). The

electronic density n_e is calculated from the emission measure (Table 3) and corresponding emitting volume V. For the latter, we assume a spherical volume with a radius R_{av} averaged between semi-major and semi-minor axes. It results in $n_e = 1.9\,(\pm0.4) \times 10^{-3} f^{-1}$ cm^{-3} for the `vapec` model, and $n_e = 1.2\,(\pm0.1) \times 10^{-3} f^{-1}$ cm^{-3} for the `vpshock` model, with f the filling factor of the plasma within the volume ($f \leq 1$). Thus, it is clear that MCSNR J0507−6847 is expanding in a rarefied medium. Still, given the size of the shell, the total swept-up mass $M_{sw} \propto n_e V$ within it is large, ranging from $881\,(\pm190)\,f^2 M_\odot$ to $M_{sw} = 557\,(\pm54)\,f^2 M_\odot$ for the `vapec` and `vpshock` models, respectively. Even accounting for a small-filling factor f, M_{sw} is much in excess of the ejecta and circumstellar material mass for any type of progenitor, and is therefore dominated by ambient ISM, justifying the assumption of a Sedov phase. The SN explosion energy is set by the size of the shell R, the plasma temperature kT_s (which depends on the shock speed), and the ambient density as $E_0 \propto kT_s R_{av}^3 n_e$. We found $E_0 = 1.0\,(\pm0.3) \times 10^{51} f^{-1}$ erg and $E_0 = 0.9\,(\pm0.2) \times 10^{51} f^{-1}$ erg for the `vapec` and `vpshock` models, respectively. This is close to the canonical 10^{51} erg for an SN and thus consistent with the interpretation of the energetics of MCSNR J0507−6847 being dominated by a single SN. Finally, the dynamical age of MCSNR J0507−6847 $t_{dyn} \propto R_{av}(kT_s)^{-1/2}$ is in the range 55 to 63 kyr in the collisional ionization equilibrium case, and between 43 and 54 kyr for the non-equilibrium case, as the temperature is slightly higher. MCSNR J0507−6847 is one of the oldest LMC SNRs, as expected at such a large size. The derived ambient density, explosion energy, and age of the SNR are consistent with the estimates of Chu et al. (2000).

Given the large size, low density, and complete shell morphology, Chu et al. (2000) suggested that the SNR was located in the near side of the LMC halo. Here, we suggest another possibility. The NGC 1850 cluster, which is located at the same position is a double cluster comprising a large globular-like cluster separated from a smaller, younger compact cluster, known as NGC 1850B, by ∼30 (e.g. Robertson 1974; Fischer, Welch & Mateo 1993; Gilmozzi et al. 1994). The ages of both clusters have been determined in various studies. Gilmozzi et al. (1994) determined ages of 50 ± 10 Myr and 4.3 ± 0.9 Myr for the main cluster and NGC 1850B, respectively. Other studies are in general agreement, with estimates ranging from 40–100 Myr for the main cluster and 1–10 Myr for NGC 1850B (e.g. Fischer et al. 1993; Vallenari et al. 1994). Mass estimates for NGC 1850 are $\sim10^4$–$10^5\,M_\odot$ (Fischer et al. 1993; McLaughlin & van der Marel 2005), placing it among the most massive in the LMC outside 30 Dor. Given the age of the main NGC 1850 cluster, the massive stellar population has already been lost to SNe, and there are no stars remaining that are capable of photoionizing the N103 shell. Rather, the young massive stars of NGC 1850B are responsible (Fischer et al. 1993; Ambrocio-Cruz et al. 1997). However, in its infancy, the main NGC 1850 cluster would have been a powerhouse, containing a significant massive stellar population, more than capable of driving a large superbubble into the ISM. To explain the low ambient density inferred for the SNR, we propose the following scenario: (i) the main NGC 1850 cluster created and powered a superbubble in the region; (ii) the evolution of this superbubble stalled after ∼40 Myr when the massive stellar population was lost and the internal pressure dropped below the ISM pressure, leaving the large, low density superbubble relic; (iii) NGC 1850B formed near the main cluster and its massive stars are now photoionizing part of the original superbubble shell, which we know as N103; and (iv) the SNR progenitor exploded in the interior of the superbubble relic created by the NGC 1850 main cluster. We also note that NGC 1850 and N103 are projected against the inside edge of the supergiaint shell SGS5 (Kim et al. 1999) and the initial superbubble could have blown out into this region. In any case, the proposed scenario can explain the very low ambient density into which the SNR has evolved.

4.3 A new BeXRB-SNR association?

Using *ROSAT* observations, Chu et al. (2000) identified a compact source at the center of MCSNR J0507−6847 superposed on the star cluster HS122. This was proposed to be a BeXRB based on its coincidence with a star-cluster region, although no timing or spectral analysis could be performed to understand its nature. The position of the compact source proposed in Chu et al. (2000) is compatible with the now known quasar MQS J050736.44-684751.6, which overlaps with the SNR along the line of sight. The other point source in the vicinity, XMMU J050722.1−684758 has been identified as a BeXRB pulsar instead in this work which qualifies as the most probable compact object associated with MCSNR J0507−6847. It is likely that XMMU J050722.1−684758, owing to its intrinsic X-ray variability, was in a faint state during the *ROSAT*observations presented in Chu et al. (2000), and thus either undetected or confused with the quasar.

For the BeXRB to be associated to the SNR requires a core-collapse origin, with the parent SN producing both the remnant and leaving an NS behind. MCSNR J0507−6847is in a star-forming region as evidenced from the presence of many upper main-sequence stars in its surrounding, and confirmed by the reconstructed star formation history by Harris & Zaritsky (2009). In a galaxy seen almost face-on like the LMC, the location of an SNR in such a star-forming region is a strong indication of a core-collapse origin, as opposed to galaxies with significant line-of-sight depth like the SMC where more confusion can arise. In the LMC, only one type Ia SNR can be clearly misidentified by looking solely at the star-forming environment of the object (Maggi et al. 2016). Coincidentally, this source is the nearby SNR N103B. Even in the absence of strong spectral evidence for a core-collapse SN, because the emission is dominated by LMC ISM, we thus conclude that MCSNR J0507−6847 was most likely created in a core-collapse SN.

Furthermore, the proximity of XMMU J050722.1−684758 near the geometrical centre of the SNR (0.9 arcsec), indicates the association of the BeXRB pulsar XMMU J050722.1−684758 with MCSNR J0507−6847. As the SNR has an almost perfect elliptical shape, the center of the ellipse is a good proxy for the likely explosion site and the origin of the NS in XMMU J050722.1−684758. This sets constraints on the NS transverse velocity. At the LMC distance of 50 kpc, the transverse velocity projected on the sky is

$$v_{proj} = 284\,\delta\theta \left(\frac{D}{50\ \mathrm{kpc}}\right)\left(\frac{t_{SNR}}{50\ \mathrm{kyr}}\right)^{-1}\ \mathrm{km\ s^{-1}} \quad (1)$$

with $\delta\theta$ the angular separation in minutes of arc from the geometric centre of the SNR to the NS, and t_{SNR} the age of the SNR. Equating this to the dynamical age t_{dyn} estimated for a Sedov model (Section 4.2, ranging from 43 to 63 kyr, and for $\delta\theta = 0.9$ acmin, the projected velocity is 200–300 km s^{-1}. The observed velocity distribution of radio pulsars indicate a mean pulsar transverse velocity of 345 km s^{-1}, with an inferred three-dimensional velocity of 450 km s^{-1} (Lyne & Lorimer 1994). The prediction for NSs in HMXBs is expected to be smaller and has diverse values in literature (on the order of 30–150 kms^{-1}; see Coe 2005; Bodaghee et al. 2012; Zuo, Li & Gu 2014; Zuo 2015). The inferred transverse velocity of the BeXRB pulsar XMMU J050722.1−684758is slightly higher than expected from the current predictions and therefore further raises a question on its association with MCSNR J0507−6847. Moreover, it

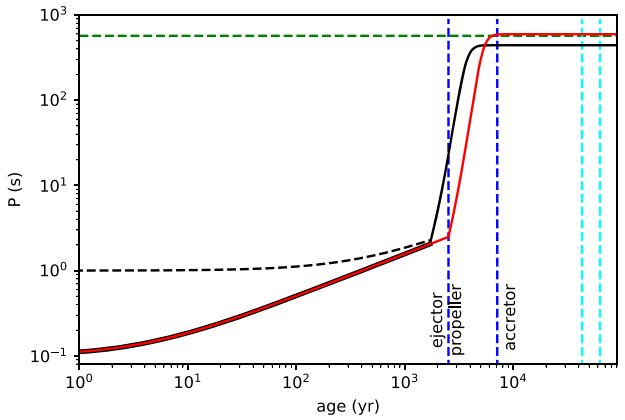

Figure 12. Spin evolution as a function of time marking the ejector, propeller and ejector phases of XMMU J050722.1−684758 following Ho et al. (2020). Assumed initial spin of the NS: P_0 is 100 ms (solid lines) and 1 s (dashed line). $B = 4 \times 10^{14}$ G and evolution is shown for a constant mass accretion rate of $\dot{M} = 8 \times 10^{-12}$ $M_\odot$ yr^{-1} (red) and 2×10^{-11} $M_\odot$ yr^{-1} (black). The green horizontal line marks the spin period and the cyan lines indicate the estimated age of the system, assuming the pulsar is indeed the progenitor of MCSNR J0507−6847.

cannot be ruled out that even if the SNR and the NS originated from the same star cluster, the progenitors of both could be distinct.

4.4 Constraints of NS properties at birth and the spin evolution of the system

Evolutionary, NSs are thought to be born with short spin periods and strong magnetic fields ($P_0 \sim 10-100$ ms, $B \sim 10^{13}$ G; Faucher-Giguère & Kaspi 2006). At birth the BeXRB pulsar is thought to be at the ejector phase. In this regime, the pulsar does not interact with the accreting matter as the NS light cylinder is smaller than the magnetospheric radius as would be calculated by the balance of magnetic and gas pressure. As the NS spins down, at some point the magnetospheric radius and light cylinder become equal and the system transitions to the propeller phase, where the interactions of the disc and magnetosphere cause a faster spin-down rate. Eventually an equilibrium is reached, however, the whole evolution is complicated by a time variable accretion rate. The duration of each phase is a function of the NS B field, and average mass accretion rate throughout the evolution. Following the prescription of Ho et al. (2020) we traced the evolutionary history of XMMU J050722.1−684758 given the estimate of the magnetic field obtained by equating the co-rotation and magnetospheric radius at spin-equilibrium:

$$P_{\rm eq} = \left(\frac{4\pi^2 R_{\rm M}^3}{G M_{\rm NS}}\right)^{1/2}, \; R_{\rm M} = \frac{\xi}{2}\left(\frac{R_{\rm NS}^{12} B^4}{G M_{\rm NS} \dot{M}^2}\right)^{1/7} \quad (2)$$

where G is the gravitational constant, $M_{\rm NS} = 1.4\,M_\odot$ and $R_{\rm NS} = 10$ km are the NS mass and radius. This results into a magnetic field of $B \sim 4 \times 10^{14}$ G. Further, from the observed L_X (i.e. $\sim 10^{35}$ erg s^{-1}) and by assuming that all dynamic energy of the in-falling material is converted to radiation we derive a mass accretion rate of 5×10^{14} g s^{-1} (i.e. $L_X \approx 0.2 \dot{M} c^2$). Using equations (7) and (12) from Ho et al. (2020), Fig. 12 plots the complete evolution of the NS spin period from the ejector phase, to the propeller phase and finally to the accretor/spin equilibrium phase when the current measured spin period of the NS is achieved. From the measured B and mass-accretion rate the system crosses the propeller stage at $t \simeq 2600$ yr and reaches spin-equilibrium at $t \simeq 7000$ yr. As is expected, the choice of the initial spin period P_0 does not affect the evolution of the system at later times, such as the accretor phase. We can obtain an upper limit on the birth spin of the NS by equating $R_{\rm M}$ with $R_{\rm LC}$ (light cylinder) and find $P_0 \lesssim 2$ s.

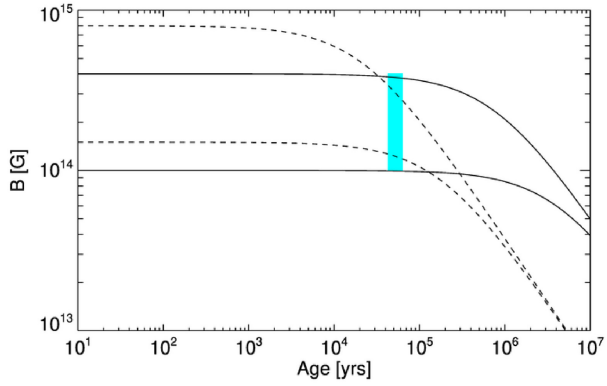

Figure 13. Magnetic field evolution assuming ambipolar diffusion in the irrotational mode (i.e. solid lines; $b = 0.01$ and $\alpha = 5/4$), or in the solenoidal mode (i.e. dashed lines; $b = 0.15$ and $\alpha = 5/4$), for different initial B field strength. The loci of the calculated B field assuming spin equilibrium for the age of the NS is marked with cyan colour.

The estimated magnetic field strength of $B \sim 4 \times 10^{14}$ G is obtained by a simple prescription of equating the co-rotation and magnetospheric radius and assuming the scaling factor between magnetospheric radius ($R_{\rm M}$) and Alfvén radius; $\xi \simeq 0.5$ (Campana et al. 2018). The B here also refers to the field measured at the magnetic poles ($\mu = BR^3/2$, where μ is the magnetic dipole moment) and the field strength measured at the magnetic equator is lower by a factor of 2. The results overall indicate a magnetar-like field strength of $B \gtrsim 10^{14}$ G.

The prescription of Ho et al. (2020) assumes a constant mass accretion rate and B throughout the various stages undergone by the system. The B on the other hand decays through non-linear processes such as ambipolar diffusion and/or a Hall cascade (Goldreich & Reisenegger 1992). Numerical simulations has shown that for $B > 10^{13}$ G this evolution follows a simple decay law (Colpi, Geppert & Page 2000), with the following form:

$$B(t) = \frac{B_0}{[1 + b\alpha B_0^{\alpha} t]^{1/\alpha}}, \quad (3)$$

where B and t quantities are in units of 10^{13} G and 10^6 yr, respectively, while values for parameters b and α denote different modes of B field decay (see Colpi et al. 2000, for details).

By following equation (3), we can calculate the B field decay from its birth and compare it with its current value (see Fig 13). It is evident that minimal decay has occurred within this time and the pulsar has maintained its initial B strength as is expected from the time-scales expected from the magnetic field decay with is $\gtrsim 10^6$ yr.

5 CONCLUSIONS

The probable association of XMMU J050722.1−684758 with MC-SNR J0507−6847 makes it the third identified BeXRB-SNR system. Pulsations are discovered at 570 s indicating the spin period of the NS. The estimated age of the SNR is 43–63 kyr which points to a middle aged to old SNR. The magnetic field strength of the NS is indicated to be $\gtrsim 10^{14}$ G. The other other such systems are SXP 1062 (Haberl et al. 2012; Hénault-Brunet et al. 2012) and SXP 1323 (Gvaramadze

et al. 2019) both located in the Small MCs. This highlights the ideal environment and the suitability of finding such objects in the MCs. All of the three BeXRB-SNR systems (including our discovery) host slowly spinning pulsars and have similar estimates for the age of the parent SNR. The eROSITA instrument on board the Russian/German SRG mission all-sky survey will provide a deep and complete coverage of the Magellanic System for the first time in X-rays and will be instrumental in finding more such systems.

ACKNOWLEDGEMENTS

This work uses observations obtained with *XMM–Newton*, an ESA science mission with instruments and contributions directly funded by ESA Member States and NASA. The *XMM–Newton* project is supported by the DLR and the Max Planck Society. GV is supported by NASA Grant Number 80NSSC20K0803, in response to *XMM–Newton* AO-18 Guest Observer Program. GV acknowledges support by NASA Grants number 80NSSC20K1107 and 80NSSC21K0213. MS acknowledges support by the Deutsche Forschungsgemeinschaft through the Heisenberg professor grants SA 2131/5-1 and 12-1. The OGLE project has received funding from the National Science Centre, Poland, grant MAESTRO 2014/14/A/ST9/00121 to AU. This work is based on data from eROSITA, the primary instrument aboard SRG, a joint Russian-German science mission supported by the Russian Space Agency (Roskosmos), in the interests of the Russian Academy of Sciences represented by its Space Research Institute (IKI), and the Deutsches Zentrum für Luft- und Raumfahrt (DLR). The SRG spacecraft was built by Lavochkin Association (NPOL) and its subcontractors, and is operated by NPOL with support from the Max Planck Institute for Extraterrestrial Physics (MPE). The development and construction of the eROSITA X-ray instrument was led by MPE, with contributions from the Dr. Karl Remeis Observatory Bamberg & ECAP (FAU Erlangen-Nürnberg), the University of Hamburg Observatory, the Leibniz Institute for Astrophysics Potsdam (AIP), and the Institute for Astronomy and Astrophysics of the University of Tübingen, with the support of DLR and the Max Planck Society. The Argelander Institute for Astronomy of the University of Bonn and the Ludwig Maximilians Universität Munich also participated in the science preparation for eROSITA. The eROSITA data shown here were processed using the eSASS/NRTA software system developed by the German eROSITA consortium. The Australian SKA Pathfinder is part of the Australia Telescope National Facility which is managed by CSIRO. Operation of ASKAP is funded by the Australian Government with support from the National Collaborative Research Infrastructure Strategy. ASKAP uses the resources of the Pawsey Supercomputing Centre. Establishment of ASKAP, the Murchison Radio-astronomy Observatory and the Pawsey Supercomputing Centre are initiatives of the Australian Government, with support from the Government of Western Australia and the Science and Industry Endowment Fund. We acknowledge the Wajarri Yamatji people as the traditional owners of the Observatory site.

DATA AVAILABILITY

X-ray data are available through the High Energy Astrophysics Science Archive Research Center heasarc.gsfc.nasa.gov. OGLE data are available through the OGLE XROM online portal http://ogle.astrouw.edu.pl/ogle4/xrom/xrom.html.

REFERENCES

Ambrocio-Cruz P., Laval A., Marcelin M., Amram P., 1997, A&A, 319, 973
Antoniou V., Zezas A., 2016, MNRAS, 459, 528
Arnaud K. A., 1996, in Jacoby G. H., Barnes J., eds, ASP Conf. Ser. Vol. 101, Astronomical Data Analysis Software and Systems V. Astron. Soc. Pac., San Francisco, p. 17
Bodaghee A., Tomsick J. A., Rodriguez J., James J. B., 2012, ApJ, 744, 108
Bozzetto L. M. et al., 2017, ApJS, 230, 2
Campana S., Stella L., Mereghetti S., de Martino D., 2018, A&A, 610, A46
Chu Y.-H., Kim S., Points S. D., Petre R., Snowden S. L., 2000, AJ, 119, 2242
Coe M. J. et al., 2012, MNRAS, 424, 282
Coe M. J., 2005, MNRAS, 358, 1379
Coe M. J., Bartlett E. S., Bird A. J., Haberl F., Kennea J. A., McBride V. A., Townsend L. J., Udalski A., 2015, MNRAS, 447, 2387
Colpi M., Geppert U., Page D., 2000, ApJ, 529, L29
Dickey J. M., Lockman F. J., 1990, ARA&A, 28, 215
Dunne B. C., Points S. D., Chu Y.-H., 2001, ApJS, 136, 119
Evans P. A. et al., 2007, A&A, 469, 379
Faucher-Giguère C.-A., Kaspi V. M., 2006, ApJ, 643, 332
Fischer P., Welch D. L., Mateo M., 1993, AJ, 105, 938
Geldzahler B. J., Pauls T., Salter C. J., 1980, A&A, 84, 237
Gilmozzi R., Kinney E. K., Ewald S. P., Panagia N., Romaniello M., 1994, ApJ, 435, L43
Goldreich P., Reisenegger A., 1992, ApJ, 395, 250
González-Galán A., Oskinova L. M., Popov S. B., Haberl F., Kühnel M., Gallagher J., Schurch M. P. E., Guerrero M. A., 2018, MNRAS, 475, 2809
Gregory P. C., Loredo T. J., 1996, ApJ, 473, 1059
Gvaramadze V. V., Kniazev A. Y., Oskinova L. M., 2019, MNRAS, 485, L6
Haberl F. et al., 2017, A&A, 598, A69
Haberl F. et al., 2020, The Astronomer's Telegram, 13609, 1
Haberl F., Sturm R., 2016, A&A, 586, A81
Haberl F., Sturm R., Filipović M. D., Pietsch W., Crawford E. J., 2012, A&A, 537, L1
Harris J., Zaritsky D., 2009, AJ, 138, 1243
Heinz S. et al., 2013, ApJ, 779, 171
Hénault-Brunet V. et al., 2012, MNRAS, 420, L13
Ho W. C. G., Wijngaarden M. J. P., Andersson N., Tauris T. M., Haberl F., 2020, MNRAS, 494, 44
Kavanagh P. J., Sasaki M., Whelan E. T., Maggi P., Haberl F., Bozzetto L. M., Filipović M. D., Crawford E. J., 2015, A&A, 579, A63
Kim S., Dopita M. A., Staveley-Smith L., Bessell M. S., 1999, AJ, 118, 2797
Kim S., Staveley-Smith L., Dopita M. A., Sault R. J., Freeman K. C., Lee Y., Chu Y.-H., 2003, ApJS, 148, 473
Kozłowski S. et al., 2013, ApJ, 775, 92
Kraft R. P., Burrows D. N., Nousek J. A., 1991, ApJ, 374, 344
Lomb N. R., 1976, Ap&SS, 39, 447
Lyne A. G., Lorimer D. R., 1994, Nature, 369, 127
Maggi P. et al., 2012, A&A, 546, A109
Maggi P. et al., 2016, A&A, 585, A162
Maggi P. et al., 2019, A&A, 631, A127
Maitra C. et al., 2019, MNRAS, 490, 5494
Maitra C. et al., 2020, The Astronomer's Telegram, 13610, 1
Maitra C., Paul B., Haberl F., Vasilopoulos G., 2018, MNRAS, 480, L136
Maitra C., Haberl F., Vasilopoulos G., Ducci L., Dennerl K., Carpano S., 2021, A&A, 647, A8
McLaughlin D. E., van der Marel R. P., 2005, ApJS, 161, 304
Predehl P. et al., 2020, A&A, 647, 16
Robertson J. W., 1974, A&AS, 15, 261
Rosen S. R. et al., 2016, A&A, 590, A1
Savitzky A., Golay M. J. E., 1964, Anal. Chem., 36, 1627
Scargle J. D., 1982, ApJ, 263, 835
Schenck A., Park S., Post S., 2016, AJ, 151, 161
Schmidtke P. C., Cowley A. P., Udalski A., 2013, MNRAS, 431, 252
Seward F. D., Charles P. A., Foster D. L., Dickel J. R., Romero P. S., Edwards Z. I., Perry M., Williams R. M., 2012, ApJ, 759, 123

Smith R. C., Points S., Aguilera C., Leiton R., Chu Y. H., Winkler P. F., MCELS, 2004, in American Astronomical Society Meeting Abstracts. p. 101.08
Souchay J., Andrei A. H., Barache C., Bouquillon S., Suchet D., Taris F., Peralta R., 2012, A&A, 537, A99
Strüder L. et al., 2001, A&A, 365, L18
Sturm R. et al., 2013, A&A, 558, A3
Turner M. J. L. et al., 2001, A&A, 365, L27
Udalski A., Szymanski M., Kaluzny J., Kubiak M., Mateo M., 1992, AcA, 42, 253
Udalski A., Szymański M. K., Szymański G., 2015, AcA, 65, 1
Vallenari A., Aparicio A., Fagotto F., Chiosi C., Ortolani S., Meylan G., 1994, A&A, 284, 447
van der Heyden K. J., Bleeker J. A. M., Kaastra J. S., 2004, A&A, 421, 1031
van Jaarsveld N., Buckley D. A. H., McBride V. A., Haberl F., Vasilopoulos G., Maitra C., Udalski A., Miszalski B., 2018, MNRAS, 475, 3253
Vasilopoulos G., Maggi P., Haberl F., Sturm R., Pietsch W., Bartlett E. S., Coe M. J., 2013, A&A, 558, A74
Vasilopoulos G., Haberl F., Sturm R., Maggi P., Udalski A., 2014, A&A, 567, A129
Vasilopoulos G., Maitra C., Haberl F., Hatzidimitriou D., Petropoulou M., 2018, MNRAS, 475, 220
Verner D. A., Ferland G. J., Korista K. T., Yakovlev D. G., 1996, ApJ, 465, 487
Watson M. G. et al., 2009, A&A, 493, 339
Wilms J., Allen A., McCray R., 2000, ApJ, 542, 914
Yew M. et al., 2020, MNRAS, 500, 2336
Zuo Z.-Y., 2015, A&A, 573, A58
Zuo Z.-Y., Li X.-D., Gu Q.-S., 2014, MNRAS, 437, 1187

This paper has been typeset from a TEX/LATEX file prepared by the author.